buildings

MDPI

Article

Anisotropy Study on the Process of Soil Permeability and Consolidation in Reclamation Areas: A Case Study of Chongming East Shoal in Shanghai

Meng Yao [1,2], Hanmei Wang [2,3], Qingbo Yu [1,2], Hui Li [4], Weitong Xia [1], Qing Wang [1,2,*], Xinlei Huang [2,3] and Jinxin Lin [2,3]

[1] College of Construction Engineering, Jilin University, Changchun 130026, China
[2] Key Laboratory of Land Subsidence Monitoring and Prevention, Ministry of Natural Resources, Shanghai 200072, China
[3] Shanghai Institute of Geological Survey, Shanghai 200072, China
[4] College of Civil Engineering and Architecture, Jiaxing University, Jiaxing 314001, China
* Correspondence: wangqing@jlu.edu.cn

Abstract: Anisotropic permeability is of great significance for assessing the consolidation and drainage mode of soil layers in reclamation areas, as well as for preventing and controlling ground settlement after project construction. This paper analyzes the anisotropic permeability of the inland and nearshore soil layers in Chongming East Shoal, Shanghai, and the formation mechanism of anisotropic permeability through permeability and scanning electron microscope (SEM) tests. The results highlight that compared with dredger fill and sandy silt, the horizontal permeability coefficient of underlying soft clay (USC) is significantly higher than its vertical permeability coefficient, which is more significant in nearshore USC. Interestingly, the upper clay (21.5 m) in the thickest clay layer shows greater anisotropic permeability than the lower clay (41.5 m). Due to the instability of seepage channels, the USC anisotropic permeability increases in a fluctuating manner as the hydraulic gradient increases. Microstructural parameters are used to reveal the mechanism of anisotropic permeability, which shows that a simple soil skeleton and structure, strong particle orientation, decreased particle abundance, increased particle roundness, decreased particle contact area, and increased pore area all contribute to the enhancement of permeability. Moreover, micro-parameters have been proposed to evaluate anisotropic permeability in terms of the effective seepage-pore area. This approach addresses the constraint of water films on the permeability efficiency of USC particles.

Keywords: land reclamation; anisotropy; permeability coefficient; microstructure characteristics; spatiotemporal variability

Citation: Yao, M.; Wang, H.; Yu, Q.; Li, H.; Xia, W.; Wang, Q.; Huang, X.; Lin, J. Anisotropy Study on the Process of Soil Permeability and Consolidation in Reclamation Areas: A Case Study of Chongming East Shoal in Shanghai. *Buildings* **2023**, *13*, 3059. https://doi.org/10.3390/buildings13123059

Academic Editor: Mengmeng Lu

Received: 25 October 2023
Revised: 4 December 2023
Accepted: 6 December 2023
Published: 8 December 2023

1. Introduction

Due to the growth of the economy and the burden of a growing population, land resources are gaining importance for coastal cities. To expand living and development space, many coastal countries or cities choose land reclamation projects, which offer the advantages of low cost and fast speed. In most cases, some cities use the sediment and waste soil near ports or waterways as potential reclamation materials to dispose of them in environmentally friendly method. This not only helps to reduce costs, but also contributes to achieving sustainable development [1,2]. As these reclamation materials are usually pumped to the designated location in the form of mud, the resulting hydraulic fill sediment usually has the engineering properties of soft clay and is highly compressible in the initial sedimentation stage, defining it as a typical soft soil [3]. In this context, if large-scale civil engineering projects are to be constructed on reclamation sites, the soft soil foundation must be strengthened prior to construction to increase the bearing capacity of the foundation. As a typical multi-level reclamation area in Shanghai, Chongming

East Shoal (CES) has implemented multiple reclamation projects since the last century. According to Shanghai land management and field investigations, newly reclaimed land can be used for engineering construction after a certain level of development [4,5]. In this regard, it is crucial to minimize the settlement of infrastructure facilities in the reclamation area after construction.

Ground settlement is closely related to soil consolidation efficiency, which is controlled by the permeability characteristics of the soil [6]. Previous studies on the permeability of cohesive soil have comprehensively considered factors such as sampling location characteristics, soil composition, clay content, external water film, soil skeleton, and pore arrangement. Different directions of soil pores and structures within the soil may breed anisotropic permeability characteristics [7,8]. As summarized by Ai et al. [9], anisotropic permeability is related to the soil structure and stratification. Meanwhile, anisotropic permeability widely exists in geomechanics (e.g., asymmetric consolidation [10]), hydrogeology (e.g., pollutant migration [11]), geological disasters (e.g., slope stability [12]), foundation pits [13], dam foundations [14], underground engineering [15], and uneven settlement/subsidence [16], etc. Therefore, anisotropic permeability is a crucial factor affecting water flow or other transport media in geotechnical engineering, particularly for the artificial surface hydraulic-fill soil and its underlying soil layers in typical multi-stage reclamation areas.

In general, the permeability anisotropy ratio is a widely used parameter to describe the anisotropic permeability characteristics of soil. This parameter is determined by the ratio of horizontal permeability (K_h) to vertical permeability (K_v) [17]. Yu [18] believed that the permeability anisotropy of cohesive soil is mainly constrained by three factors: macroscopic stratification, microscopic stratification, and the preferential orientation of particle aggregates. Zhou et al. [19] found a nonlinear positive correlation between the permeability anisotropy of remolded kaolin and axial stress under constant K_0 conditions. For Boston Blue Clay, Adams et al. [20] discovered that an increase in consolidation stress contributed to an increase in permeability anisotropy. Wang and Qiu [21] reported that the smaller the nonuniformity coefficient of soil particles, the smaller the permeability anisotropy ratio. Therefore, it is comparatively simple to quantify the permeability anisotropy of soil from a macroscopic perspective. In fact, permeability anisotropy is closely related to the microstructure of soil. Hence, research on microstructures can help to establish the interaction between the soil microstructure and macroscopic behavior, as well as to reflect the impacts of natural and artificial factors on the internal microstructure of soil.

The microstructure of soil plays an important role in anisotropic permeability, which has garnered significant attention from scholars [22,23]. Some hypotheses related to anisotropic permeability have also been proposed, including the development of capillary force [24], the specific surface-area ratio of particles/pores [25], the control of matrix suction on the permeability of unsaturated soil [26], and changes in the pore network model caused by flowing medium [27]. Xu et al. [28] claimed that anisotropic permeability stems from the anisotropy of the microstructure, which comprises the soil skeleton, particle connections, particle contact relationships, particle orientation, and pore morphology. In fact, these factors are interdependent in the soil microstructure, enabling qualitative and quantitative descriptions of the anisotropic permeability behavior of soil. Horpibulsuk et al. [29] found that the structure of low-expansive clay became more flocculated with an increase in ion concentration in the pore solution, thus improving its water-holding capacity. Clennell et al. [30] underscore the impact of the particle aggregation effect and the microstructure heterogeneity of clay particles as key factors that restrict the development of anisotropic permeability. According to Yang and Aplin [31], the intact mudrock had an anisotropy ratio range of 1.2–1.9, where a higher permeability anisotropy ratio indicates stronger soil layer heterogeneity. Pusch and Yong [32] found that the interaction between clay particles and water (i.e., pore fluid) may further lead to the development of different types of microstructures (i.e., the spatial arrangement of particles). Interestingly, some microstructural models have even been used to capture the influence of particle or

pore geometry on permeability anisotropy, such as Daigle and Dugan [33], who derived a geometric model to calculate the tortuosity of the seepage path for the average particle orientation, particle aspect ratio, and porosity. Based on the above model, Adams et al. [20] explained the response of plate-like particle arrangements to the permeability anisotropy of mudrock. Clearly, the evaluation mechanism of micro-scale anisotropy is helpful for further understanding the macroscopic anisotropic permeability behavior of soil.

Inspired by the aforementioned research, this study aims to explore the micro-mechanisms of the permeability anisotropy in different soil layers of a typical multi-level reclamation area in CES. Considering the influences of the time effect and burial depth on the permeability anisotropy, soil samples from drillings of near-inland (1949–1964) and near-shore (1990–2001) areas were selected for comparative analysis. Meanwhile, the variations of K_h and K_v of different soil layers under a multi-level hydraulic gradient were analyzed. Moreover, considering the effect of the exterior water film of particles on permeability constraints, an appropriate microscopic parameter has been established to evaluate the anisotropy of permeability in viscous soils.

2. Materials and Methods

2.1. Study Area

Chongming Island (121°10′–121°54′ E, 31°27′–31°51′ N) is the largest alluvial sand island in China. Due to its unique geographical location and water–sediment environment, Chongming Island began to form and gradually developed into its current pattern in 618–626 AD [34]. CES is located at the eastern end of Chongming Island, near the intersection of the Yangtze River and the Yellow Sea (Figure 1a). Historically, CES has undergone multiple reclamation projects, and it has rapidly expanded from west to east. Each reclamation project is bounded by embankments built in adjacent years, mainly in 1949, 1964, 1976, 1990, 1998, 2001, and 2015 (Figure 1b). Referring to the guidelines of the Chinese Code for the Investigation of Geotechnical Engineering [35], we arranged boreholes in the inland reclamation area (1949–1964) and offshore reclamation area (1990–2001) for sampling so as to obtain the soil-layer property parameters under the space–time pattern of different reclamation stages. To facilitate comparative analysis, the borehole depth was uniformly limited to 55 m, with each soil layer within 55 m having at least one sample. Offshore boreholes were sampled at relatively consistent intervals, with sampling intervals of 2 m. A total of 34 undisturbed soil samples were collected through field investigations. Unlike urban centers, the typical strata of CES has very thick Holocene clay deposits [18]. Geological ages and soil types [36,37] were used to identify the main soil layers in CES, from top to bottom as follows: ① 3-2 dredger fill (DF); ② 2-3 sandy silt (SS); ③ muddy clay (MC); ④ 1-1 clay; ⑤ 1-2 silty clay (SC) (Figure 1c). The dredger fill was a gray or grayish-yellow soil layer that was artificially deposited. Visible plant roots were present inside the dredger fill, as shown in Figure 1d. The sandy silt exhibited similar geotechnical characteristics to the dredger fill, with heterogeneous soil and local intercalation of gray soft plastic (organic-containing) clay or dense shell layers. The underlying soft clay (USC) included muddy clay, clay, and silty clay, which are typical compression layers with obvious sedimentary structures, distinct slip and viscous feels, and a fishy odor. The soil samples were immediately sealed with wax and wrapped with several layers of plastic film to avoid water evaporation and disturbance after collection. Vibration was avoided during transportation to ensure the integrity of the soil sample, and then laboratory analysis was conducted.

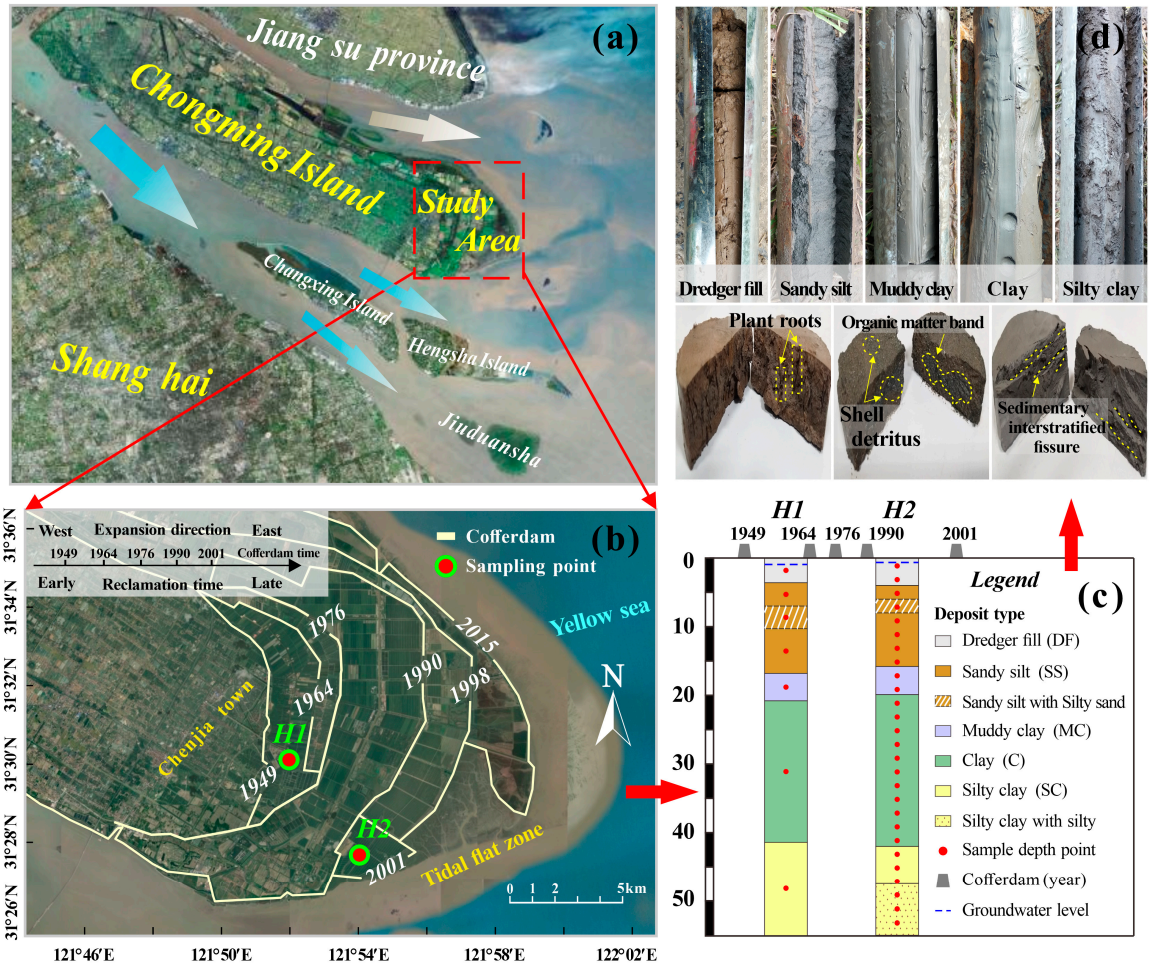

Figure 1. (**a**) Location map of CES; (**b**) The spatiotemporal evolution of the CES reclamation area and the layout of the sampling holes; (**c**) Layout of the stratigraphic structure and sampling depth of inland and offshore boreholes; (**d**) Representative soil sample photos.

2.2. Basic Properties

In this study, the basic properties of these soil samples, including the natural moisture content, dry density, porosity, and organic matter content, were tested according to the Standard GB/T 50123-2019 soil-testing method [38], as shown in Figure 2a–d. The water content of dredger fill and sandy silt were similar, ranging from 27.98% to 32.46%, whereas that of the USC ranged from 31.3% to 51.17%. The dry density of dredger fill and sandy silt ranged from 1.44 g/cm^3 to 1.55 g/cm^3, whereas that of the USC ranged from 1.20 g/cm^3 to 1.41 g/cm^3, indicating that coarse-grained soils tend to be more tightly packed than fine-grained soils. The variation pattern of the pore ratio and the natural water content is similar, with the porosity of dredger fill and sandy silt ranging from 0.74 to 0.91, and that of the USC ranging from 0.95 to 1.39. In addition, the organic matter content of each soil layer was less than 1.5%, with the dredger fill having a slightly higher organic matter content, indicating that the complex composition of dredger fill and its diverse sources provide a certain organic-matter accumulation environment.

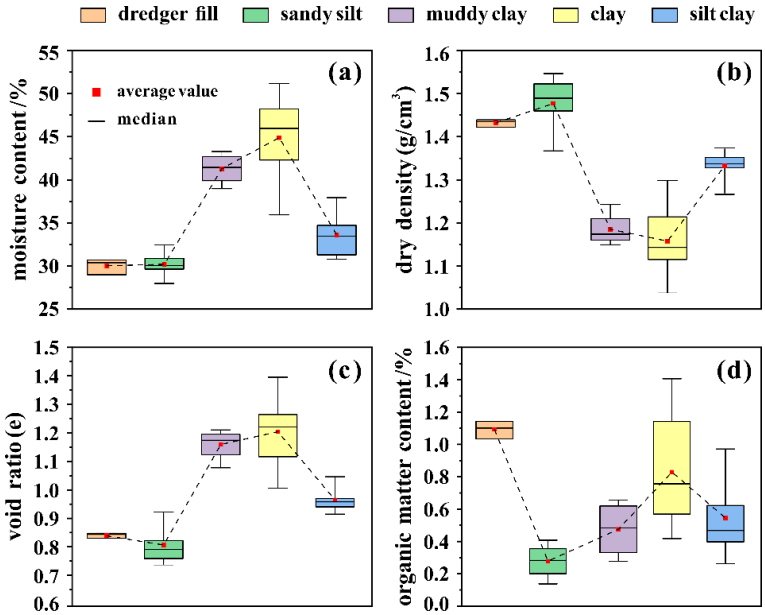

Figure 2. The physical and chemical characteristics derived from routine tests of the main geological samples, including the (**a**) natural water content; (**b**) dry density; (**c**) void ratio; and (**d**) organic matter content.

The grain size distribution was determined by using a laser particle-size analyzer (BT9300LD) as described by [39]. The particle-size classification referred to the Standard GB/T 50123-2019 soil-testing method [38]. In all soil samples, the proportion of silt was highest, followed by that of clay (Figure 3a). As a natural sedimentary soil layer with a longer history, USC has a more stable particle-size distribution than dredger fill and sandy silt. Referring to the SY/T 5163-2010 Standard [40], the *K*-value method was used for the quantitative analysis of XRD, and the results are shown in Figure 3b,c. The quartz content in each soil layer dominated (>45%), while the content of other primary minerals was generally less than 10%. Secondary clay minerals were mainly illite-mixed layer and illite, with small amounts of kaolinite and chlorite. The widespread deposition of chlorite reflects a marine sedimentary environment [41].

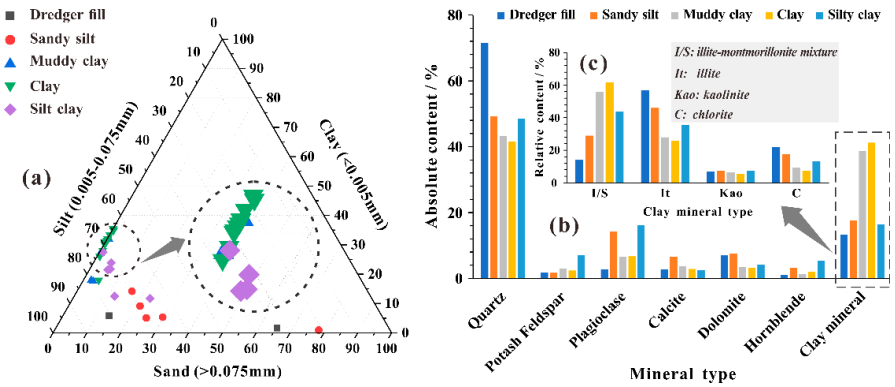

Figure 3. Testing of material composition, including (**a**) particle-size composition and (**b**,**c**) mineral composition.

2.3. Test Methods

Standard ring-cutter samples with a height of 2 cm were selected as the test samples, as shown in Figure 4a. The permeability test referred to the Standard GB/T 50123-2019 soil-testing method [38]. The saturated hydraulic conductivity (*K*) of the samples was measured using a variable-head automatic permeameter (LFTD-1406), as shown in Figure 4b,c. The

required hydraulic gradient was generated by adjusting the water-column height, and after the water-head height was stable, the data were automatically collected and processed using the accompanying software to calculate the permeability within the range of hydraulic gradient changes. K can be calculated using Equation (1). Each hydraulic gradient was conducted in 3–5 parallel tests until the allowable error value did not exceed 2×10^{-N} cm/s (where N represents the order of magnitude of the soil sample permeability), and then the next hydraulic gradient test was performed.

$$K_v = 2.3\frac{aL}{At}log\frac{\triangle H_1}{\triangle H_2} \quad (1)$$

where a is the cross-sectional area of the hydraulic-head measurement tube, a = 0.785 cm^2; L is the length of the permeation path, i.e., the height of the soil sample, L = 2 cm; A is the cross-sectional area of the ring cutter, A = 30 cm^2; t is the permeation time (s); $\triangle H_1$ and $\triangle H_2$ are the initial and final hydraulic-head heights (cm) during the test, with H_1's initial height being uniformly set to 50 cm. It should be pointed out that in order to standardize the results, the K at water temperature T °C is uniformly converted to the K at 20 °C (K_{20}), as shown in Formula (2):

$$K_{20} = K_T\frac{\eta_T}{\eta_{20}} \quad (2)$$

where η_T is the viscosity coefficient of water at T °C (kPa·s); η_{20} is the viscosity coefficient of water at 20 °C (kPa·s). Since the samples were prepared both horizontally and vertically (Figure 4a), K_h represents the saturated horizontal permeability, while K_v represents the saturated vertical permeability. Based on the measured values of K_h and K_v, the permeability anisotropy coefficient (PAC) can be calculated using the following formula [42–44]:

$$PAC = lg(\frac{K_h}{K_v}) \quad (3)$$

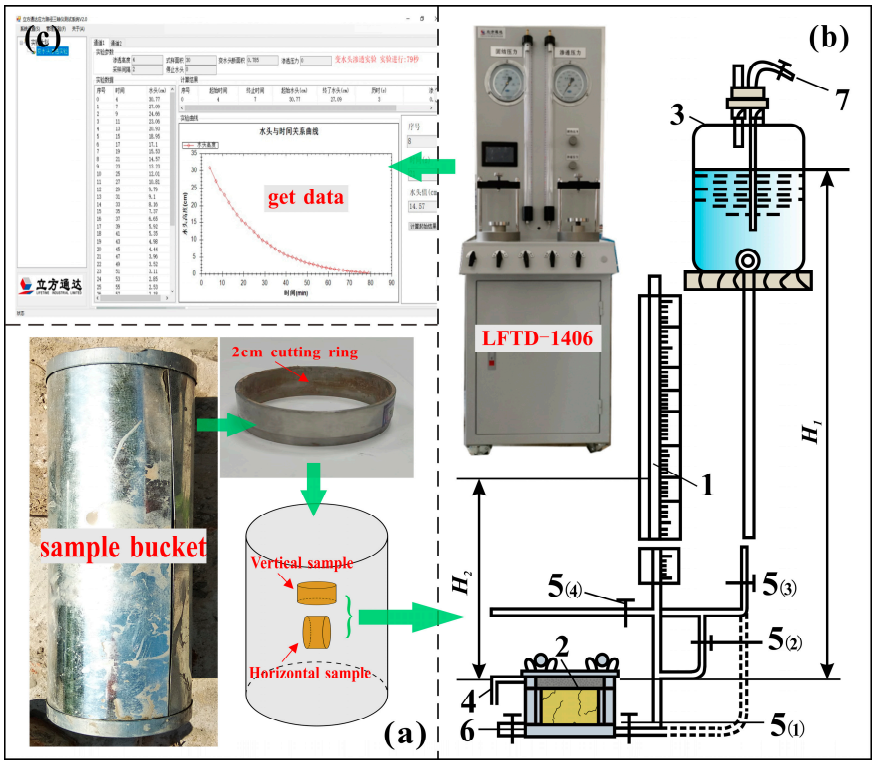

Figure 4. Permeability test process. (**a**) Preparation of the test soil samples; (**b**) Schematic diagram of the penetration instrument device; (**c**) Obtaining the data.

If PAC > 0, then $K_h > K_v$; if PAC < 0, then $K_h < K_v$; if PAC = 0, then $K_h = K_v$.

A scanning electron microscope (Phenom ProX) was used to observe the microstructural characteristics of the soil samples (Figure 5e). To reduce the volume and microstructural changes caused by water loss, the samples required a freeze-drying pre-treatment (Figure 5a–c). After that, a thin layer of gold was sputtered onto the sample surface (Figure 5d) to improve the image quality.

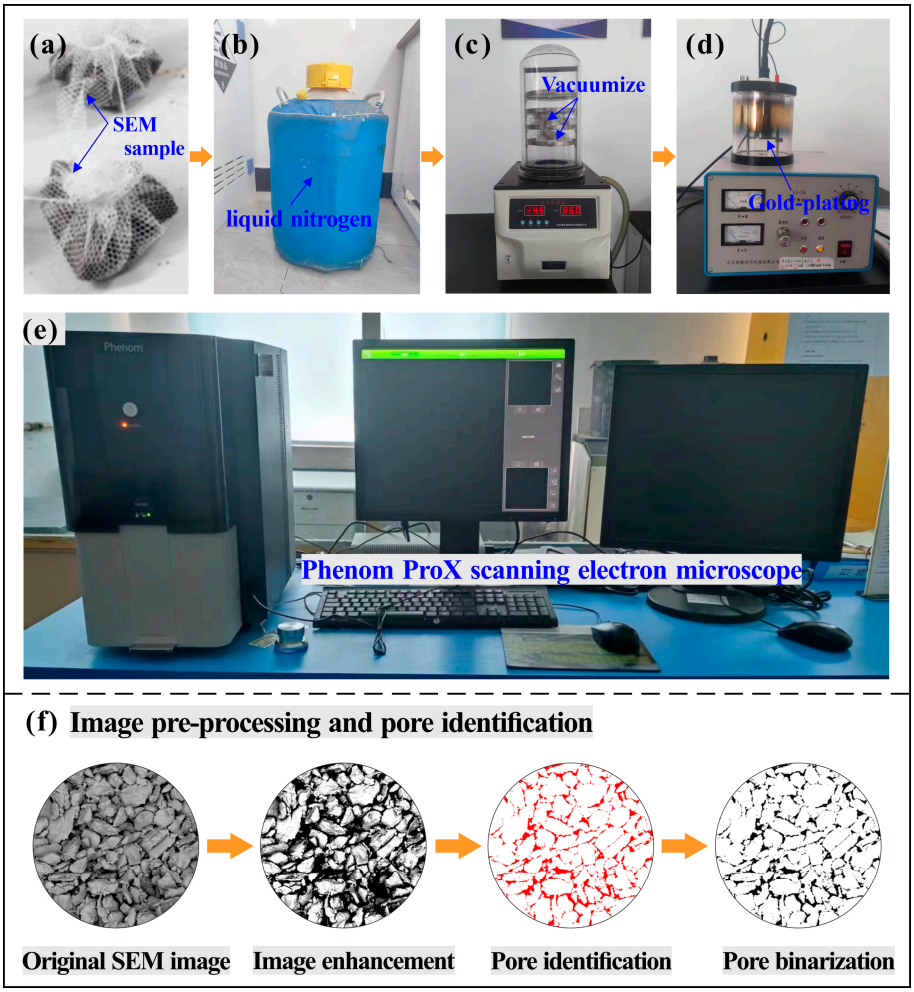

Figure 5. (**a**–**e**) Test procedure and instrument equipment; (**f**) IPP 6.0 identification process for pores.

IPP6.0 was used for the image data acquisition (Figure 5f). First, the SEM image was preprocessed, including adjusting the brightness and contrast, removing noise, etc. [45]. Among these, median filtering could blur small-scale details in the image and better reduce the noise interference. The threshold method was used to segment the particles and pores, and selection of the threshold was based on a combination of image histogram distribution and experience. Following the selection of the threshold, the grayscale image was binarized, hence dividing it into two regions: white, representing particles, and black, representing pores. Afterward, the microscopic parameters of the segmented particles or pores, including the pore area, particle orientation angle, particle abundance, particle roundness, etc., can be quantified.

3. Results

3.1. Anisotropy Characteristics of Permeability in Soil Layers of Different Depths

To investigate the variation in permeability anisotropy with depth, the horizontal and vertical permeability coefficients of each soil layer were measured using the soil profile obtained from an offshore borehole, which is representative of the overall area. The test results

are summarized in Figure 6. The permeability coefficients of different soil layers exhibit significant variations in the order of magnitude. The horizontal permeability coefficients of dredger fill and sandy silt range from 1.99×10^{-5} cm/s to 1.69×10^{-2} cm/s, whereas the vertical permeability coefficients range from 1.76×10^{-5} cm/s to 1.77×10^{-2} cm/s. The horizontal and vertical permeability coefficients of USC are in the order of 10^{-7} cm/s. Nevertheless, upper clay has stronger permeability than lower clay; for instance, the ratio of K_h (21.5 m)/K_h (41.5 m) is approximately 1.96, and the ratio of K_v (21.5 m)/K_v (41.5 m) is about 1.25.

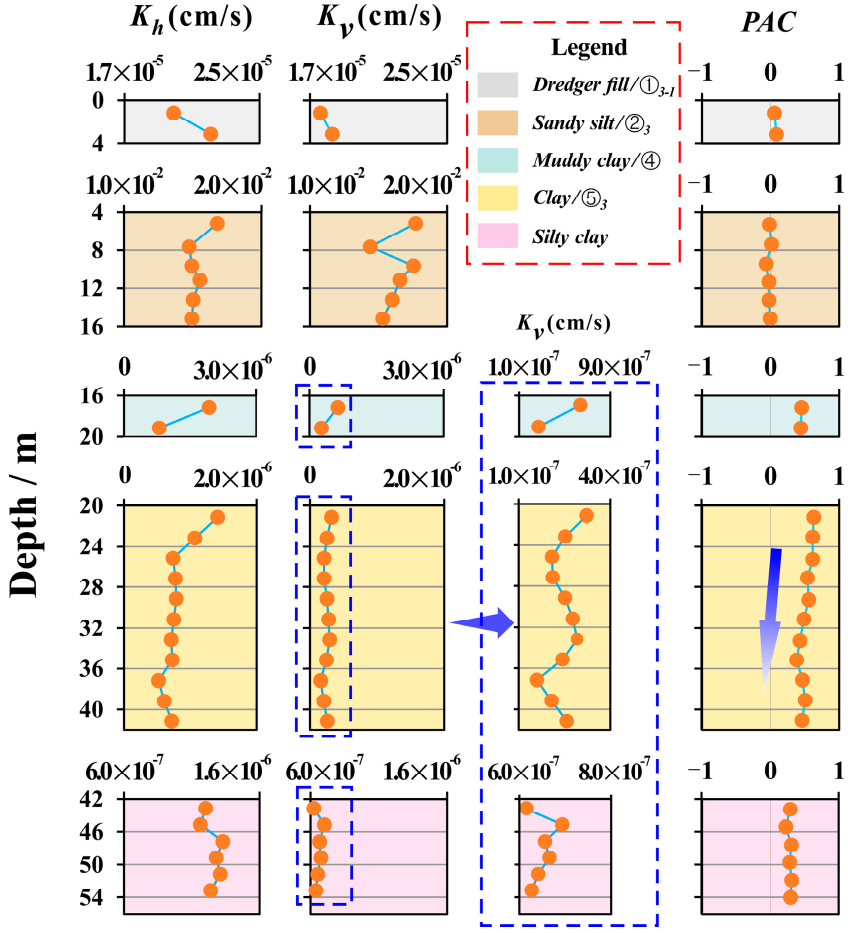

Figure 6. The variation of K_h, K_v, and PAC with depth.

Based on the K_h and K_v results, the PAC was calculated using Equation (3), as shown in Figure 6. The nonzero value of the PAC for each soil layer implies the presence of permeability anisotropy in these soil layers. The average PAC values of dredger fill and sandy silt, muddy clay, clay, and silty clay are 0.068, −0.023, 0.475, 0.515, and 0.279, respectively, indicating that the permeability anisotropy of USC is relatively prominent. On a macroscopic scale, the layered sedimentary cracks and the horizontal distribution of thin sand layers between the soil layers in USC may be a major reason for the higher K_h than K_v values (Figure 1d). In addition, for the thickest clay layer, the PAC generally decreases with the burial depth increases, which means that the dominance of K_h gradually weakens. Similar findings were reported by Li and Zhang [46]. They observed that with an increase in vertical stress, fine particles within the clay progressively infiltrate the macropores, resulting in their initial destruction or complete disappearance. Hence, the compacting effect of the upper layers on the soil beneath can weaken the permeability anisotropy of the soil in both horizontal and vertical directions.

3.2. Permeability Anisotropy of Soil Layers during Different Reclamation Periods

Land reclamation has had multiple effects on the sedimentary environment of underlying soil layers [47]. Therefore, comparing the permeability differences of different layers during different reclamation periods can help to further understand the spatial and temporal variability of soil permeability characteristics and their relationship with permeability anisotropy. Figure 7a'–e' show the PAC changes in the soil layers for the inland borehole profile (1949–1964) and the nearshore borehole profile (1990–2001). The PAC calculation involves using the average K_h and K_v values for each soil layer. It is noticeable that the PAC of the same-depth soil layer in the early reclamation is generally smaller, which is more evident for USC. Ma et al. [48] suggested that strong sedimentary environment differences lead to significant permeability anisotropy of the soil in different directions, and the increase in pore connectivity in the vertical direction due to particle densification is the primary cause of the weakening of the permeability anisotropy. Song et al. [49] suggested that the decrease in permeability anisotropy of the same soil layer is related to the flocculent structure formed by the sedimentation process of the soil itself. In fact, due to the loose arrangement of particles in dredger fill and sandy silt, water infiltration in the soil pores under complex geological conditions is stochastic, and vertical and horizontal pores provide almost equal conditions for water flow. However, USC originates from layered sedimentation. Influenced by sedimentary environment and artificial fill loads, the increase in overlying soil pressure makes it easier for pores to be compacted horizontally than vertically. Consequently, as the sedimentation time of USC increases, the decrease in K_h becomes more prominent, and the permeability anisotropy weakens (Figure 7a–e).

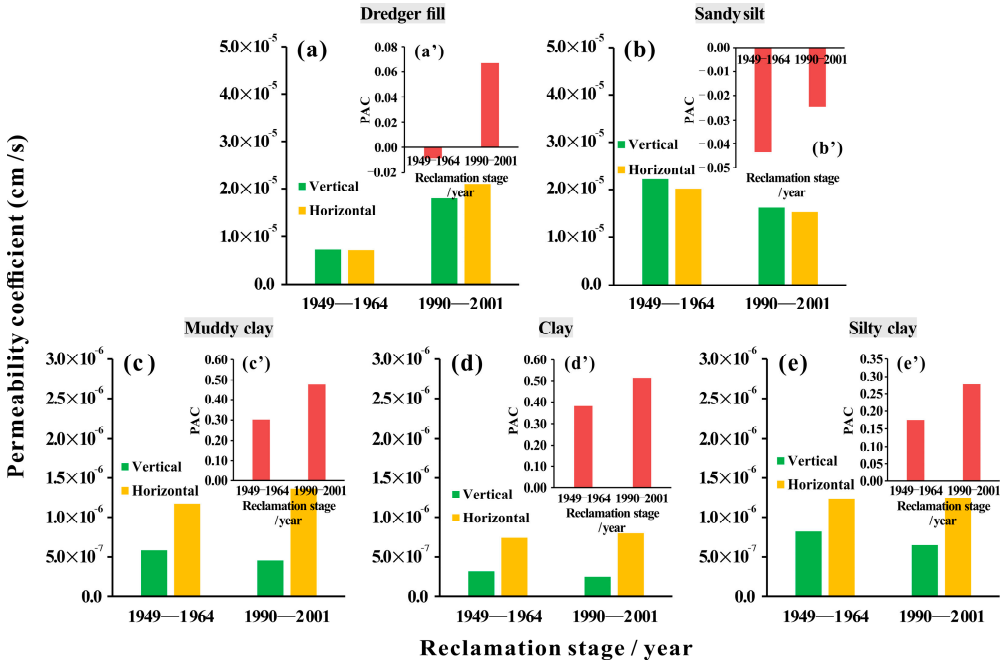

Figure 7. (**a'–e'**) Changes in the PAC with reclamation time; (**a–e**) Changes in the K_h and K_v values of different layers with reclamation time.

3.3. Permeability Anisotropy of Different Soil Layers under Different Hydraulic Gradients

As the burial depth of soil varies, the height of the water pressure it is subjected to also varies. Therefore, it is imperative to explore the relationship between the permeability anisotropy of each soil layer and the hydraulic gradient. Figure 8 displays the fluctuations in the PAC with regard to hydraulic gradients. In detail, as the hydraulic gradient increases, the PAC of the nearshore dredger fill fluctuates between 0.088–0.093. However, the PAC of the inland dredger fill decreases, indicating that K_h and K_v are gradually approaching each other (Figure 8a). When $i > 55$, the PAC of the inland dredger fill becomes negative, indicat-

ing that as the hydraulic gradient exceeds a certain critical value, the vertical permeability of the inland dredger fill gradually becomes dominant. For the sandy silt, the PAC of the nearshore is higher than that of the inland. Apart from a small reduction in the inland PAC in the range of 25–35, the PAC of both the nearshore and the inland generally increases gradually with an increasing hydraulic gradient (Figure 8b). The PAC of muddy clay, clay, and silty clay shows a similar pattern with the hydraulic gradient, that is, when the water head increases, the PAC generally shows an increasing trend (Figure 8c–f). However, there is a fluctuating pattern in the PAC increase trend for USC, which could be due to the instability of permeable channels caused by the infiltration process [50]. Interestingly, when $i > 45$, the PAC of inland silty clay is higher than that of nearshore silty clay. This could be caused by the mixed components of the silty clay, such as the interbedded silt layer in the silty clay layer (Figure 1d); the different soil properties result in varying permeability.

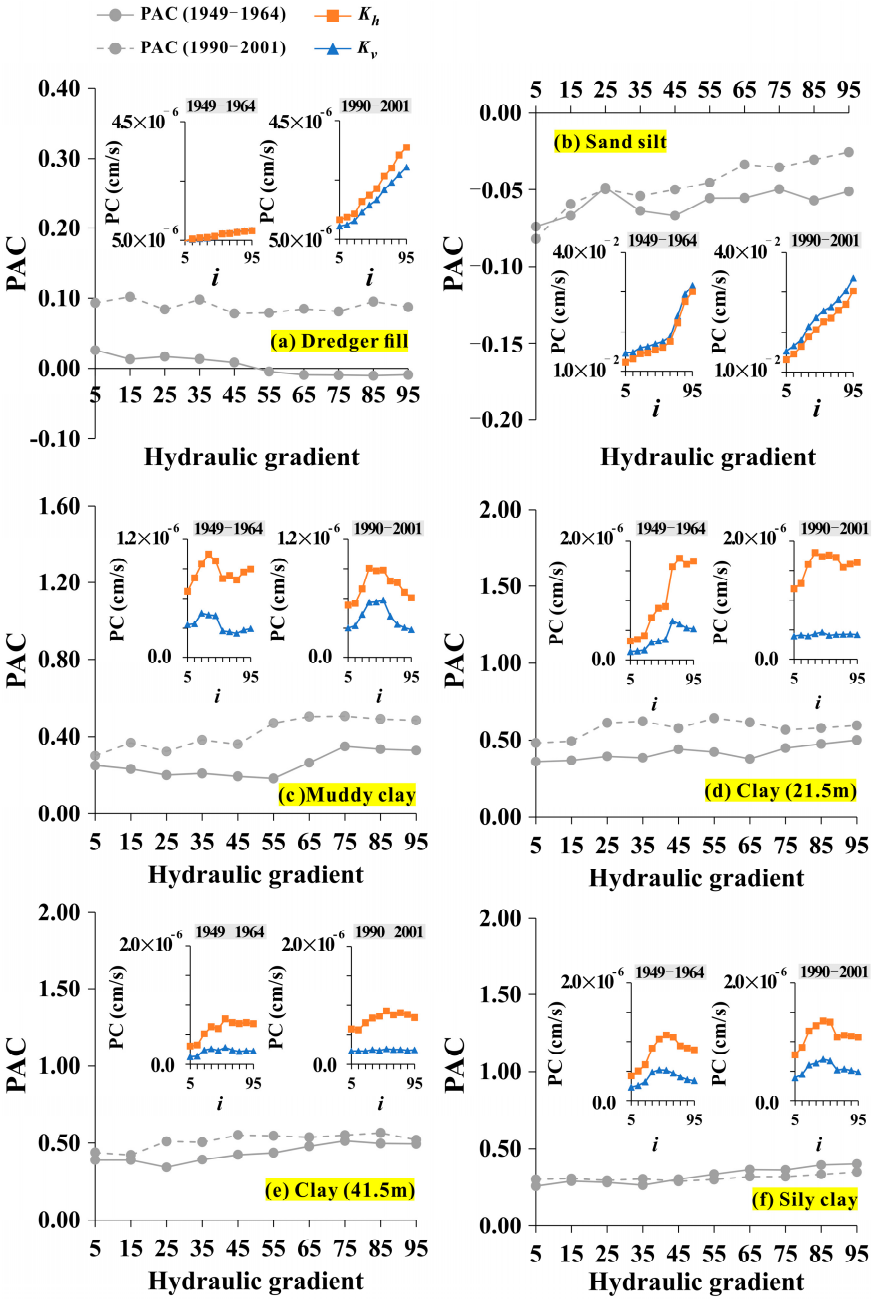

Figure 8. (**a**–**f**) Variations in K_h, K_v, and PAC values with hydraulic gradients in different layers of inland and offshore areas.

3.4. Differentiation of Microstructures in Different Directions

For the qualitative description of the microstructure, representative micrographs of each soil layer from the near inland and nearshore borehole profiles were selected. The SEM images were used to present the microstructure of the undisturbed soil samples at a high magnification (2000×) (Figure 9). The analysis of SEM images mainly focuses on microstructure types, surface characteristics of particles, particle arrangements, particle contact modes, and pore types.

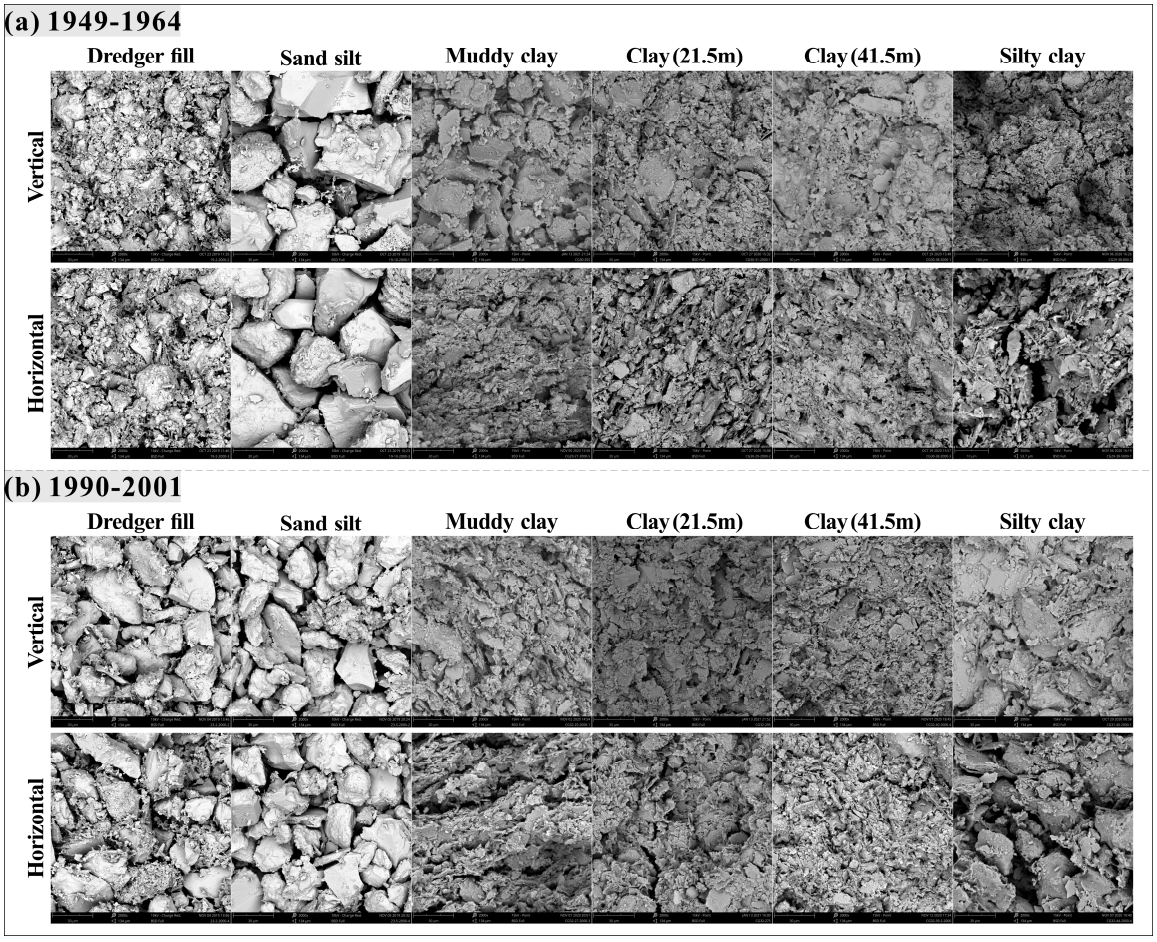

Figure 9. (**a**,**b**) Vertical and horizontal SEM images of different soil layers during different reclamation periods.

Dredger fill exhibited similar microstructural features in both the vertical and horizontal directions, namely a skeletal structure. The outlines of the coarse particles were relatively distinct, with small particles distributed in a star-shaped pattern on the surface of the coarse particles or embedded between them. There was no apparent orientation of particles based on their arrangement. Additionally, the primary contact modes between particles were mainly point-to-point and point-to-surface, allowing for the visual observation of intergranular pores.

The microstructural characteristics of sandy silt and dredger fill were analogous, both demonstrating a skeletal structure. In contrast to dredger fill, sandy silt exhibited a cleaner surface of coarse particles in both the vertical and horizontal orientations, without evident directional characteristics of the particles. The contact modes between the particles were primarily point-to-point and point-to-surface, resulting in the prevalence of intergranular pores.

Muddy clay is a transitional soil layer between silty soil and cohesive soil, with a relatively thin soil layer and a flocculent microstructure. From different directions of the soil

sample, the muddy clay exhibited a more obvious anisotropic structure in the vertical and horizontal directions, mainly reflected in the high directionality of its horizontal particles or aggregates. The layered deposition of cohesive soil during the geological structure process may be the main reason for this phenomenon [51]. In addition, the particle contact mode was edge–surface contact, and the pore type was the coexistence of intergranular pores and intragranular pores.

The clay layer, being the thickest stratum within the sampling depth, exhibited an agglomerated structure. It contained a lower content of coarse particles, and fine particles were aggregated in the form of flocculation or agglomeration, giving rise to small pores between particles or units. This was a direct contributing factor to its poor permeability. Similar to muddy clay, the horizontal particles of the clay layer also exhibited distinct orientation characteristics, leading to a directional arrangement of pores. The contact modes of the particles were edge-to-face and face-to-face, and both intergranular and intragranular pores coexisted.

Silty clay, as the soil layer with the highest burial depth, also had strong permeability anisotropy, which was similar to that of muddy clay and clay. It was not difficult to see that, compared with the vertical direction, the obvious locally banded penetrating cracks in the horizontal direction were the key factor for its obvious permeability advantage in that direction. In addition, the contact modes of the particles were edge–surface and surface–surface contact, with visible intergranular pores and intragranular pores.

4. Discussion

4.1. The Influence of Particle Orientation on Permeability Anisotropy

The directionality of particles has a significant effect on the permeability of soil [52]. To characterize the particle orientation of each soil layer sample, the IPP6.0 software was used for microscopic image processing. The particle orientation was divided into 18 groups, with a counting interval of 10°, to draw a rose diagram, as shown in Figure 10. When the frequency of a certain interval is higher, it indicates that more structural units have similar directionality, and the overall orientation of soil particles will be enhanced, and the fluctuation degree of the orientation frequency will also increase. Figure 10a reflects the particle orientation of the vertical and horizontal samples of the dredger fill, indicating insignificant directional characteristics. The original structure of the dredger fill sand is severely destroyed due to the combined effects of artificial stacking and external forces, leading to an internally disorganized arrangement of structural units. Figure 10b depicts the particle orientation of the vertical and horizontal samples of sandy silt. As the adjacent soil layer underlying the dredger fill, while the sandy silt has not undergone the process of artificial handling, due to its similar particle-size composition to dredger fill (Figure 3) and its relatively weak bonding ability between powder particles, the particles may tend to be oriented toward a certain angle during the permeation process. This is reflected in the high coincidence of particle orientation angles in the vertical and horizontal directions of the sandy silt, which are mainly concentrated at 60–120°.

Figure 10c–f illustrate the directional distribution of particles in USC. Compared with the vertical direction, the horizontal particle orientation angles in the USC exhibit a more preferred distribution in terms of quantity. Although the direction angles of these particles are not fixed in a certain specific range, this suggests a noticeable occurrence of particle rearrangement in USC during the permeation sedimentation process. Meanwhile, the strong directionality exhibited by particles in the USC is related to their own structural instability. The infiltration consolidation effect of natural sedimentation drives the fine particles inside the USC to be easily entrained by the water flow, especially in nearshore USC. This is due to the short time of the overlying soil layer for land formation, leading to the insufficient draining and consolidation effect from the overlying soil pressure on the USC itself. From a micro-scale perspective, this may be related to the loose flocculation and agglomerated structure of nearshore USC (Figure 9).

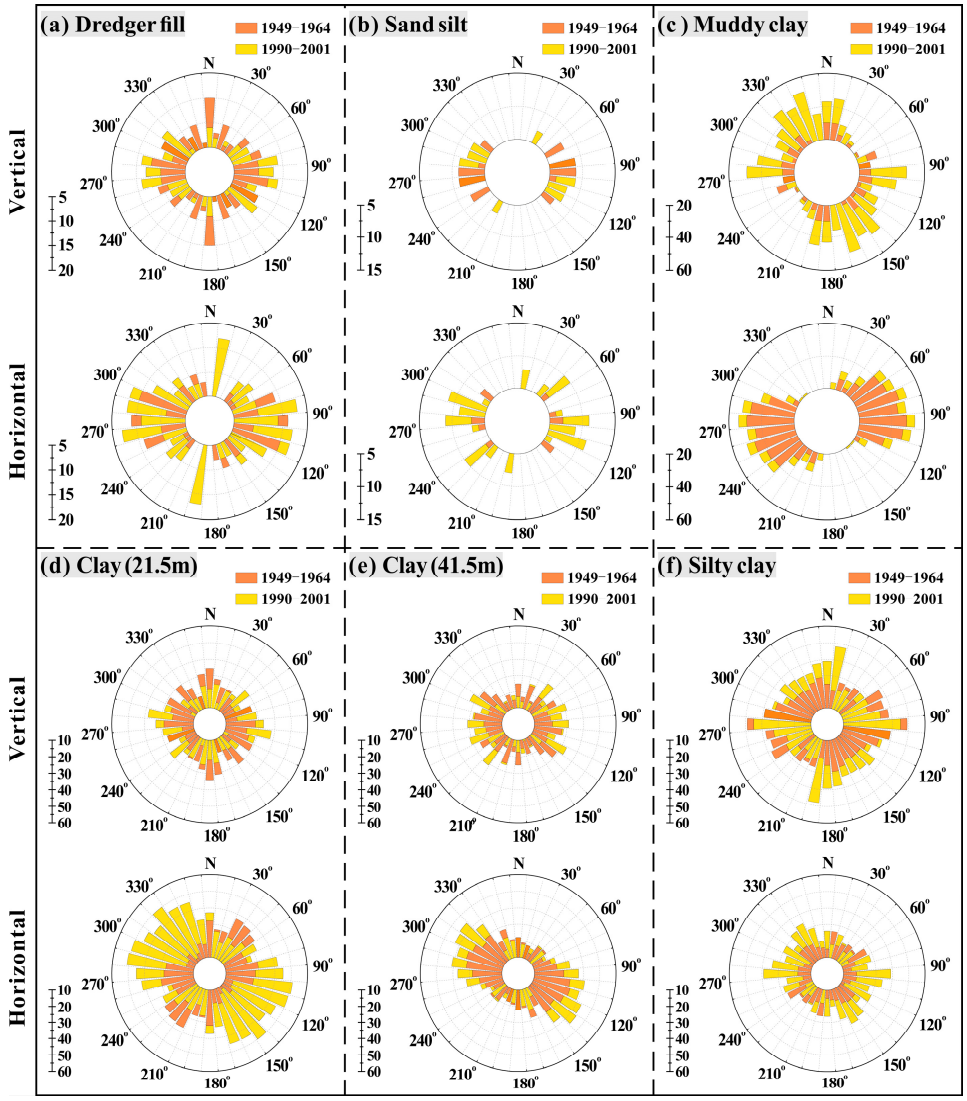

Figure 10. (**a**–**f**) Rose plots of the particle orientation in different layers of samples.

4.2. The Influence of Particle Morphology on Permeability Anisotropy

Soil permeability can be affected by the shape of particles. Abundance is used to identify the shape of soil particles, which is defined as the ratio of short to long axes of particles or units [17,53]. Statistical results of soil particle abundance are shown in Figure 11a,b. In Figure 11a, it can be observed that the abundance of most particles generally follows the normal distribution pattern. The dominant abundance in USC is always concentrated around 0.5, while the dominant abundance range of dredger fill and sandy silt seems to be more extensive, exhibiting "multi-peak"-type (e.g., DF-Vertical-1949~1964; DF-Horizontal-1990~2001) or "platform"-type (e.g., SS-Horizontal-1949~1964; SS-Horizontal-1990~2001) distribution. In Figure 11b, the average abundance of dredger fill and sandy silt is found to be higher than that of USC. This suggests a positive correlation between abundance and particle size, that is, the coarser the particles, the larger the abundance. Moreover, the average abundance of vertical and horizontal particles in the same stage of the dredger fill and sandy silt is approximately equal. However, the abundance of USC horizontal particles is slightly higher than that of vertical particles; this finding is consistent with the fact that particle abundance can be used as a reference for sorting the strength of permeability in different directions [54].

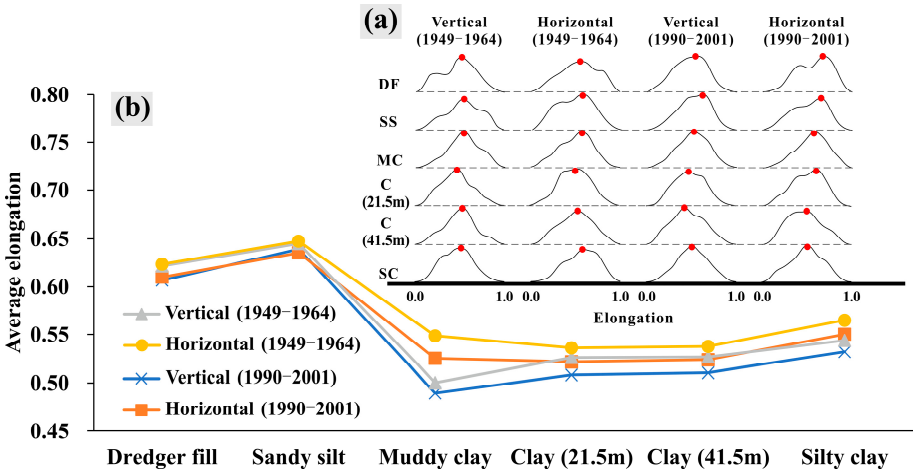

Figure 11. (**a**,**b**) Particle Abundance of Samples from Different Strata.

Furthermore, changes in particle abundance resulting from time effects have distinct characteristics [55]. Inland samples have a higher average particle abundance compared with offshore samples, but this difference is not significant in dredger fill and sandy silt. Although the shape of the particles is more influenced by their original source area (and properties) than their migration history, the limited variation in this attribute is believed to be inherently related to the content of small particles in sediment [56]. USC, which has a larger burial depth and an increase in clay content compared with dredger fill and sandy silt, provides a higher water-head gradient internally under saturated conditions. With an increase in sedimentation time, the shape of large particles is subjected to strong hydraulic erosion, and the collision between migrated small particles causes great wear on the external morphology. Xu et al. [57] also suggested that changes in particle morphology caused by mechanical collisions may be related to high gradient hydraulic pressure. Particle migration distance is another factor that cannot be ignored. USC has a larger sedimentary thickness, and due to the increase in particle shape sorting and the migration distance, the particle morphology undergoes significant changes under a hydraulic drive. This is another important reason why the difference in the vertical and horizontal abundance of USC is higher than that of dredger fill and sandy silt.

Conceptually, particle roundness is related to the relative roundness or angles (sharpness) of the edges and corners of the particles [58], which is defined as the ratio of the actual area of a particle or structural unit to its circumscribed circle area. Roundness depends on the physical characteristics of the particles themselves (shape, size, etc.) and the preferred orientation and contact mode of the microstructure that is composed of soil particles [59], which can indirectly reflect the permeability of the soil to some extent. Although roundness is widely used to describe particle shape, there is no unified standard for its classification interval. Typically, particle roundness is divided into six levels: very angular, angular, sub-angular, sub-rounded, rounded, and well rounded. This paper adopts the classification method of roundness proposed by Powers [60], which has been accepted by other scholars [61]. The specific classification intervals are shown in Table 1.

Table 1. The classification intervals of roundness proposed by Powers (1953) [60].

Powers (1953)	Unnatural Particles	Very Angular	Angular	Sub-Angular	Sub-Rounded	Rounded	Well Rounded
Roundness	0.00–0.12	0.12–0.17	0.17–0.25	0.25–0.35	0.35–0.49	0.49–0.70	0.70–1.00

Overall, both the vertical and horizontal particles of each soil layer are mainly angular, sub-angular, and sub-rounded, while the percentage of very angular, rounded, and well-rounded particle content is less than 18%. Sub-rounded particles are relatively concentrated

in the dredger fill and sandy silt, with a maximum percentage of 41.55%. Conversely, subangular particles dominate in USC. Therefore, the average particle roundness of dredger fill and sandy silt is higher than that of USC. From different directional angles, the average particle roundness of the vertical and horizontal directions of dredger fill and sandy silt is relatively close, while the vertical average particle roundness of USC is significantly lower than its horizontal average particle roundness (Figure 12), indicating that roundness is positively correlated with the permeability coefficient. As revealed in Figure 9, the dredger fill and sandy silt form a soil skeleton by overlapping silts and a small amount of clay, unlike the agglomeration and flocculation of USC. This structure leads to poor cohesion between particles after moistening; hence, under relatively low critical hydraulic gradients, particles are easily eroded by water. Camenen [62] found that pore water-flow velocity can be an important factor in controlling soil particle roundness in similar studies.

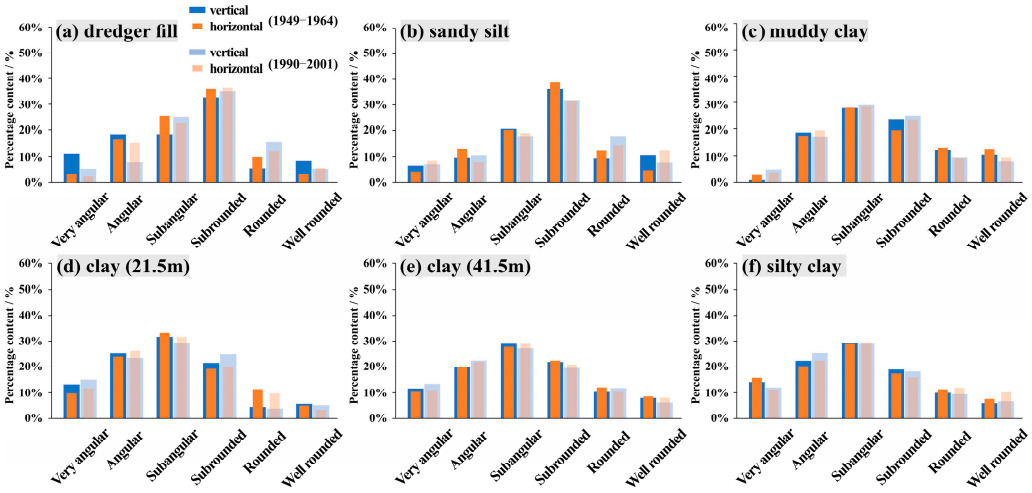

Figure 12. Distribution of particle roundness levels in samples from different layers.

At the same time, USC benefits from the directional arrangement of particles and local banded cracks in the horizontal direction (Figure 9), making this direction the preferred choice for seepage behavior. Under the dual effects of water-flow erosion and particle collision, it is relatively easy for horizontal particles in the USC to be rounded. This hydraulic–mechanical synergy can also be confirmed in the average roundness of soil samples from different backfill stages. The particle roundness of inland soil samples is slightly superior compared with offshore soil samples (Figure 13). Therefore, larger particle roundness may promote pore-channel connectivity, which, in turn, further promotes particle rounding in enlarged seepage pores. There exists a positive or negative feedback relationship between pore structure and particle roundness, and these factors will ultimately be coupled in the particle arrangement, particle connection, pore size, and other aspects.

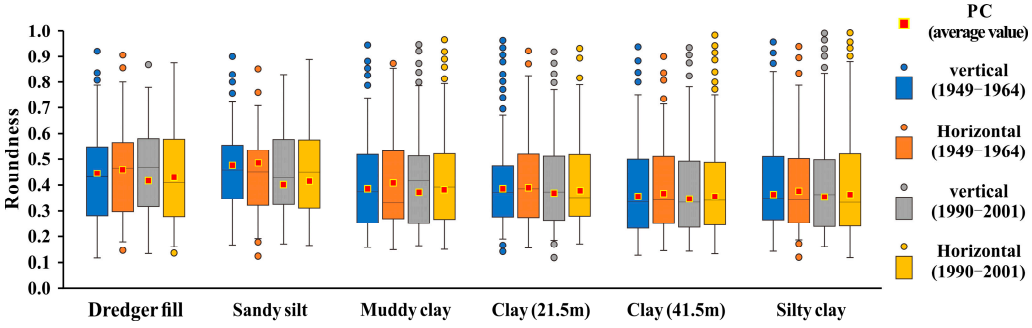

Figure 13. Comprehensive statistics of particle roundness in samples from different layers.

4.3. The Influence of Pore Area on Permeability Anisotropy Coefficient

4.3.1. Proposal of New Parameters

Pore characteristics play an important role in determining the soil permeability and permeability anisotropy. According to the development trend of *e*-log*K*, the K_h and K_v of each soil layer are positively correlated with the void ratio (Figure 14a–e). However, the correlation between K_v, the K_v of USC, and the void ratio is slightly weaker. The correlation coefficient R^2 for linear fitting ranges between 0.7174 and 0.7827 for K_v and the void ratio, while that of K_h and the void ratio ranges between 0.6137 and 0.6316. Some scholars have confirmed that the pores in cohesive soil can be divided into effective flow pores and ineffective flow pores [63,64]. Ineffective flow pores are usually divided into non-connected pores, micro-connected pores, and connected pores that cannot transmit pore water, with the third type of pore mainly occupied by bound water. Bound water on the surface of soil particles has high viscosity and poor fluidity and cannot transfer pore water pressure, which especially obstructs the permeability of cohesive soil. However, measuring the thickness of bound water on the soil particle surface is challenging, and no optimal method has been identified. Cui et al. [65] found the thickness of the weakly bound water film on clay particle surfaces to be approximately 0.12 μm through experiments without adding the ion soil stabilizer ISS solution. They believed that water could flow freely in pores only when the pore radius exceeds twice the thickness of the weakly bound water film. With regard to this, the article suggests that pores with a diameter exceeding 0.24 μm can be considered effective seepage pores. Considering the structural characteristics of the soil itself, this paper simplifies the seepage path as circular pore seepage within micro-tubes [66]. Specifically, in the two-dimensional SEM, pores with an area exceeding 0.045 μm^2 (S = πr^2) are deemed effective seepage pores.

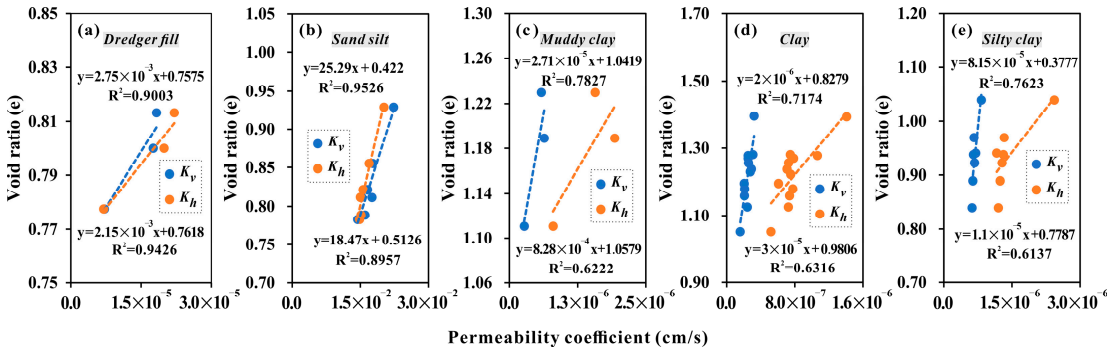

Figure 14. (**a**–**e**) Relationship between the pore ratio and the permeability coefficient of samples from different layers.

The effective flow pore-area percentage was defined as the ratio of pores with an area larger than 0.045 μm^2 to the total pore area in SEM images of USC soil samples. Based on this, the following parameters were defined.

(1) Anisotropic coefficient of the effective seepage-pore area

Referring to the computation formula for the PAC, the logarithm of the ratio of the horizontal effective flow pore area to the vertical effective flow pore area was defined as the "anisotropic coefficient of effective seepage-pore area", as shown in Equation (4).

$$\gamma_p = \lg\left(\frac{S_h}{S_v}\right) \tag{4}$$

where γ_p is the anisotropic coefficient of the effective seepage-pore area, S_h is the horizontal effective seepage area, and S_v is the vertical effective seepage area.

(2) Anisotropic coefficient of the effective seepage-pore-area weight

The ratio of the effective flow pore area to the total pore area is defined as the effective seepage-pore-area weight. Based on this, the logarithm of the ratio of the horizontal effective seepage-pore-area weight to the vertical effective seepage-pore-area weight was defined as the "anisotropic coefficient of effective seepage-pore-area weight", as shown in Equation (5).

$$\gamma_{pw} = \lg(\frac{P_h}{P_v}) \quad (5)$$

where γ_{pw} is the anisotropic coefficient of the effective seepage-pore-area weight; P_h is the horizontal effective seepage-area weight, and P_v is the vertical effective seepage-pore-area weight.

By using the above formulas, microscopic parameters were obtained for each sample in the 1949–1964 and 1990–2001 soil layers, and the results are shown in Tables 2 and 3, respectively.

Table 2. Microscopic parameters of soil samples from 1949 to 1964.

Soil Type	Direction	Total Pore Area/μm^2	Effective Seepage Area/μm^2	Effective Seepage Area Percentage/%	γ_p	γ_{pw}
MC	vertical horizontal	701.25 744.44	523.02 559.10	74.58% 75.10%	2.90×10^{-2}	3.02×10^{-3}
C (21.5 m)	vertical horizontal	717.59 763.19	542.57 581.07	75.61% 76.14%	2.98×10^{-2}	3.01×10^{-3}
C (41.5 m)	vertical horizontal	659.02 692.48	498.92 525.51	75.71% 75.89%	2.26×10^{-2}	1.04×10^{-3}
SC	vertical horizontal	624.16 677.23	475.67 525.08	76.21% 77.53%	4.29×10^{-2}	7.48×10^{-3}

Table 3. Microscopic parameters of soil samples from 1990 to 2001.

Soil Type	Direction	Total Pore Area/μm^2	Effective Seepage Area/μm^2	Effective Seepage Area Percentage/%	γ_p	γ_{pw}
MC	vertical horizontal	681.36 711.95	505.19 531.79	74.14% 74.69%	2.23×10^{-2}	3.21×10^{-3}
C (21.5 m)	vertical horizontal	693.17 720.43	503.36 527.41	72.62% 73.21%	2.03×10^{-2}	3.52×10^{-3}
C (41.5 m)	vertical horizontal	644.19 665.56	443.35 460.72	68.82% 69.22%	1.67×10^{-2}	2.52×10^{-3}
SC	vertical horizontal	638.60 673.22	494.48 529.24	77.43% 78.61%	2.95×10^{-2}	6.58×10^{-3}

Overall, the proportion of S_h in USC is better than that of S_v, which is consistent with the result that the K_h of USC is higher than that of the K_v. Meantime, the proportion of S_h and S_v in USC ranges from 68.82% to 78.61%, indicating that although bound water films on the surface of USC particles occupy a certain pore area, the effective seepage-pore area remains relatively high. Furthermore, since γ_p and γ_{pw} are based on the ratio of S_h and S_v, the larger the absolute value of these two coefficients, the greater the difference between S_h and S_v. According to Tables 2 and 3, the γ_p and γ_{pw} values for silt clay are slightly higher than those for muddy clay and clay, which may be related to the horizontal interlayer cracks caused by the layered deposition (Figure 9). For the clay layer with the greatest thickness, the γ_p and γ_{pw} values for the upper clay (21.5 m) are slightly higher than those for the lower clay (41.5 m), indicating that as the depth increases, the advantage of K_h over K_v gradually weakens. According to Pires et al. [67] and Jiang et al. [68], the structure of the lower soil layer can become denser as the overlying soil pressure increases with depth. Permeability anisotropy is influenced by stresses acting in various directions on the soil skeleton. From

the perspective of soil skeleton units, the horizontal stress on the skeleton units at the same depth is equal and can be offset, whereas the vertical direction, as the direction of geological subsidence, is dependent on the overlying pressure and gravity. The horizontal-plane soil skeleton units perpendicular to the direction of geological subsidence are relatively easy to compress. Beyond a certain burial depth, when the overlying pressure surpasses the soil skeleton's resistance, the soil skeleton unit's shape alters considerably, accompanied by the elimination of certain horizontal pores, resulting in a serious weakening of the horizontal effective permeability capacity.

Figure 15 illustrates the degree of attenuation of the horizontal and vertical permeability coefficients for the lower clay layer (41.5 m) relative to the upper layer of clay (21.5 m). The decay of K_h is consistently greater than that of K_v, particularly in offshore clays. Therefore, the preferential attenuation of the permeability coefficients of the lower soil layer due to the overlying soil pressure may have directionality and timeliness [42,69], and the sensitivity of horizontal pores to soil deformation may be higher in offshore clays.

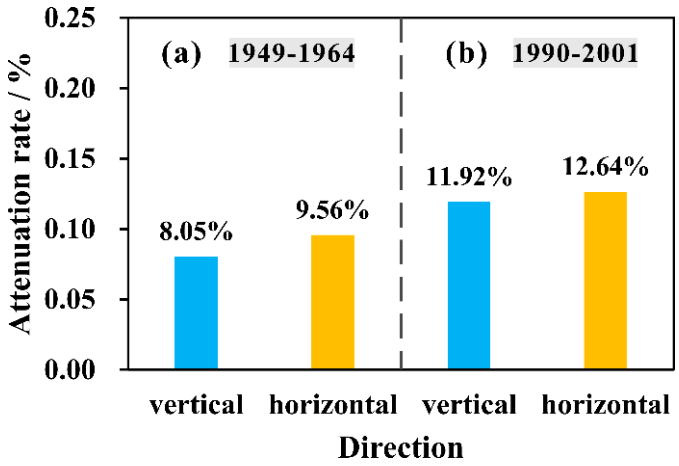

Figure 15. Attenuation degree of the permeability efficiency of deep clay relative to shallow clay at different stages of reclamation.

4.3.2. Applicability Analysis of New Parameters

To demonstrate the reasonableness and applicability of the parameters γ_p and γ_{pw}, the clay (21.5 m) from the filling stage between 1990 and 2001 was selected as the representative sample. The SEM images of the samples after permeation for hydraulic gradients of i = 5, i = 35, i = 65, and i = 95 were observed, and the pore parameters were obtained using IPP 6.0, as shown in Figure 16.

As the hydraulic gradient increases, the effective flow pore area of offshore clay (21.5 m) increases in both the horizontal and vertical directions (Figure 16). Meanwhile, as the hydraulic gradient increases, the fitting lines of γ_p and γ_{pw} display an increasing trend, which is consistent with the results of the PAC with the increase in the hydraulic gradient, indicating that the proposed parameters γ_p and γ_{pw} are applicable to explaining the intrinsic mechanism of the permeability anisotropy of clay. Interestingly, although the slope of the fitting line of γ_p and γ_{pw} is similar to that of the hydraulic gradient, the fitting degree of γ_p is better, and the goodness-of-fit, R^2, reaches 92.5% (Figure 17). This implies that when quantitatively analyzing the permeability anisotropy from a micro-perspective, using γ_{pw} as a variable may be more appropriate. To obtain more objective and accurate theoretical prediction results, further refinement research should be carried out on the permeability anisotropy from multiple perspectives, such as the genesis history of soil, natural environmental evolution, mechanical action mechanism, etc., coupled with factors such as particle arrangement and pore morphology of the soft clay structure to extract corresponding parameters to supplement the existing formulas.

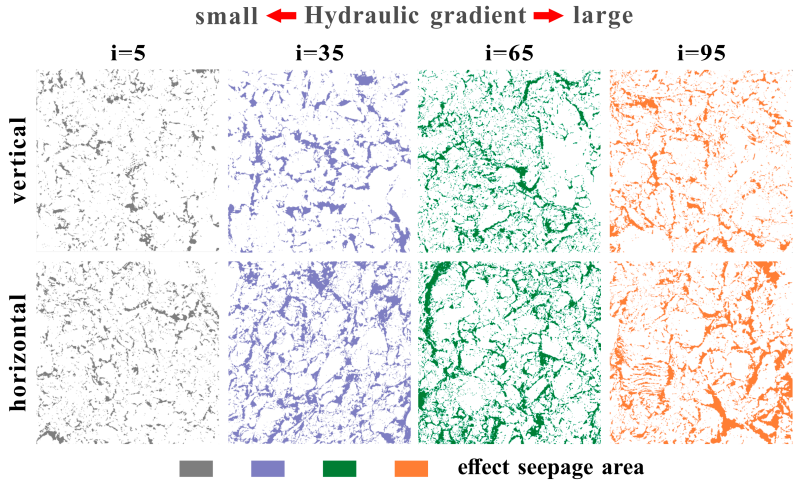

hydraulic gradient (i)	direction	Total pore area /μm²	Effective seepage area /μm²	Effective seepage area percentage / %	Υ_{pore}	$\Upsilon_{pore\text{-}weight}$	PAC
i=5	vertical	646.14	485.31	75.11%	3.09×10^{-2}	6.36×10^{-3}	0.483
	horizontal	683.66	521.06	76.22%			
i=35	vertical	691.16	526.86	76.23%	2.64×10^{-2}	1.01×10^{-2}	0.622
	horizontal	717.58	559.86	78.02%			
i=65	vertical	734.16	559.65	76.23%	4.85×10^{-2}	1.21×10^{-2}	0.615
	horizontal	798.25	625.74	78.39%			
i=95	vertical	782.79	586.11	74.87%	3.40×10^{-2}	2.02×10^{-2}	0.595
	horizontal	808.01	633.79	78.44%			

Figure 16. Variations in microscopic parameters under different hydraulic gradients.

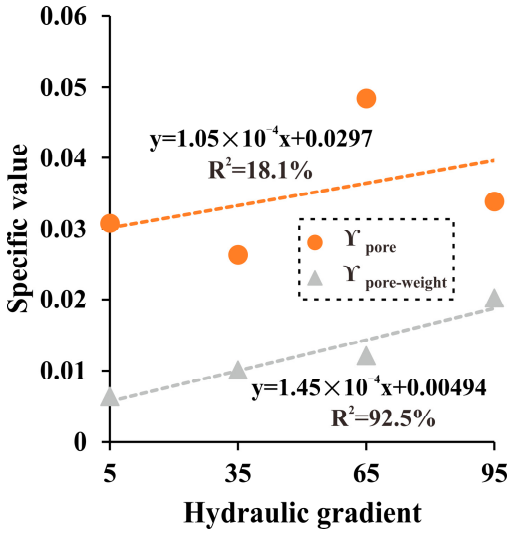

Figure 17. Variations of γ_p and γ_{pw} with the hydraulic gradient (taking the upper clay of offshore areas as an example).

4.4. Mechanism Analysis

The discussion above highlights that soil permeability is closely tied to its microstructure characteristics, while the permeability anisotropy is controlled by factors such as particle arrangement, particle contact relationships, particle shape, and effective seepage-pore area. In addition to dredger fill, sandy silt, and muddy clay, clay and silt clay are natural sedimentary soils, of which the latter three belong to the USC. Due to the influ-

ence of layered sedimentation, the horizontal arrangement of particles in the USC has orientation, which leads to directional arrangement of the pores in the horizontal direction. Meanwhile, permeability anisotropy is related to the particle shape. Compared with the rod-shaped particles in USC, the particle shape in dredger fill and sandy silt is relatively round (Figure 18a), which reduces the difference in permeability between the horizontal and vertical directions while reducing the seepage resistance.

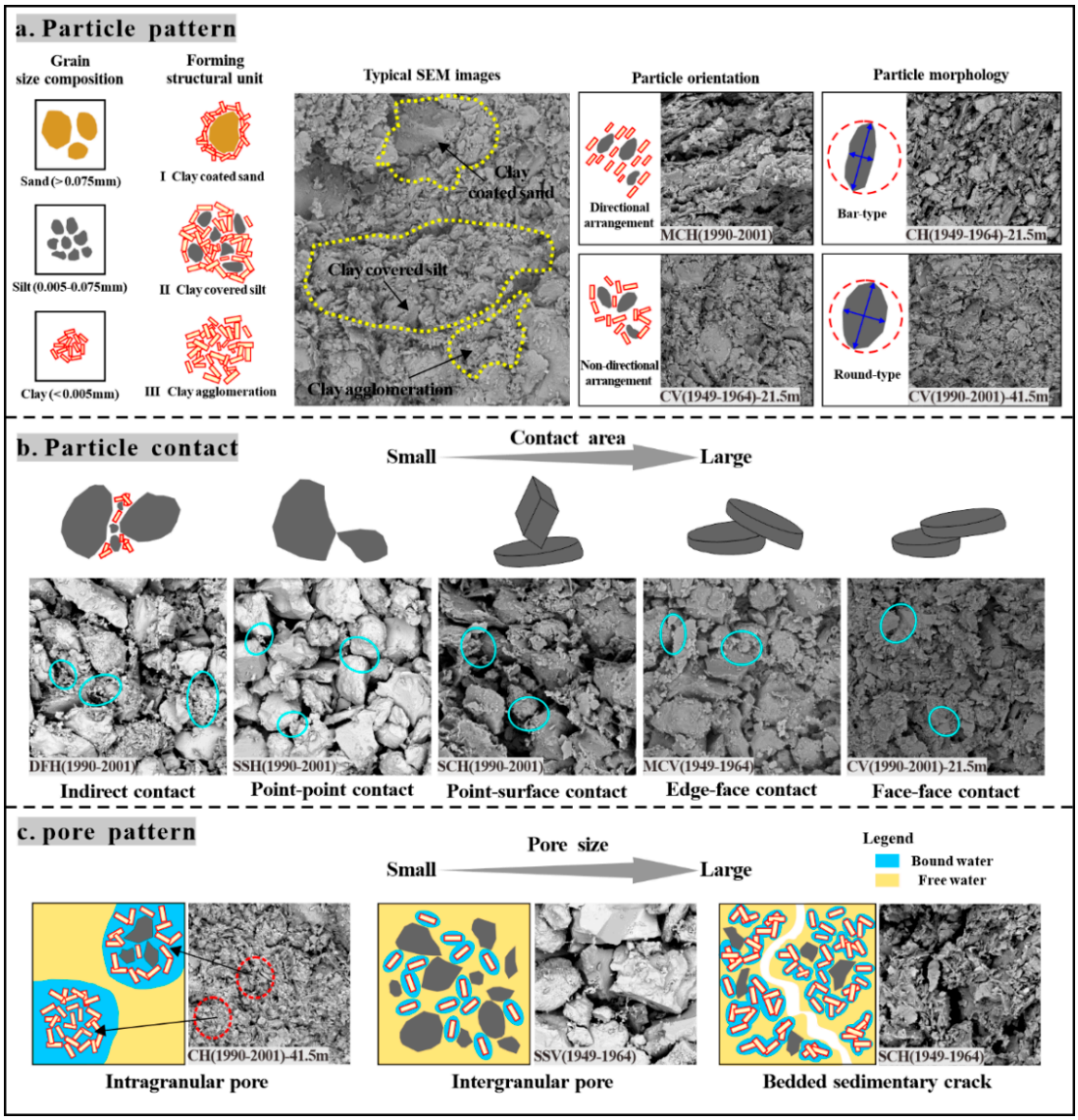

Figure 18. Microstructure model of anisotropy mechanism in each soil layer (**a**) Particle mode; (**b**) Particle contact relationship; (**c**) Pore type.

The contact mode between soil particles varies in different soil layers at different depths. Dredger fill and sandy silt have a loose structure with primarily non-direct and point-to-point contact (Figure 18b), resulting in effective horizontal and vertical drainage. USC has a prolonged sedimentation time, and the greater clay content increases the degree of particle bonding, thereby inhibiting the development of pores in USC. Therefore, USC has a lower permeability coefficient than dredger fill and sandy silt. Simultaneously, particles in USC have a relatively large contact area, mainly through point–face, edge–face, and face–face contact (Figure 18b). As the burial depth increases, the overlying soil pressure on the USC likewise intensifies, resulting in a larger contact area between particles. However, the soil skeleton experiences more severe compression in the horizontal profile than in the

vertical, as evident by the greater attenuation of S_v compared with S_h (Figure 17). Thus, for the same layer of clay, the upper clay has stronger permeability anisotropy characteristics than the lower clay.

Furthermore, pore characteristics are a critical factor that influence the permeability anisotropy. Compared with USC, dredger fill and sandy silt have slightly larger pore sizes, mainly consisting of interparticle pores (Figure 18c), which enhance the connectivity of pores in both the horizontal and vertical directions. At the same time, the pore shape depends on the shape of the structural unit. Thanks to the more obvious layered sedimentation horizontal interlayer fractures (Figure 18c), the γ_p and γ_{pw} of silty clay are slightly higher than those of muddy clay and clay.

Another important discovery is that the PAC of USC usually rises with an increasing hydraulic gradient, albeit with fluctuating trends that may be attributed to seepage channel instability. Analysis of the relationship between the hydraulic gradient and K_h and K_v in USC reveals that as the gradient increases, K_h and K_v initially increase, then decrease, and eventually stabilize (Figure 8c–f). For undisturbed USC, the gradual increase in the water-head height may drive the migration of small particles originally attached to the soil skeleton or embedded in the pores. At this stage, due to the gradual opening of pore channels, the permeability coefficient increases. However, the migration path of particles may be random, so a higher hydraulic gradient does not necessarily indicate a smoother channel for particle migration. As the hydraulic gradient continues to increase, when the accumulated number of migrating particles exceeds the drainage load of the pores, these particles will gradually accumulate in the seepage channels, resulting in the key nodes of the seepage channels being blocked and the permeability coefficient decreasing accordingly. Moreover, because of the limitations of the seepage boundary conditions, the migrating particles carried by the pore water will not be lost outside the soil indefinitely, which is the reason why the permeability coefficient eventually tends to be stable rather than continuously decreasing.

Based on the theory of effective permeable pore area, this paper proposes two new parameters: γ_p and γ_{pw}. Under the condition of multi-stage hydraulic gradient infiltration, taking the nearshore upper clay (21.5 m) as the experimental soil sample, it is speculated that γ_{pw} may be more suitable for the quantitative analysis of permeability anisotropy from a micro-scale perspective.

4.5. Engineering Implications

The reclamation of land from the sea holds immense importance for the development and utilization of coastal land resources, the transformation and protection of coastlines, and the construction of strategic infrastructure. However, the engineering properties of dredged silt are poor. Not only does it cause significant settlement after land formation, but it also compresses the underlying soil layer to varying degrees, resulting in uneven ground settlement, loss of fill elevation, secondary geological disasters, and a series of other problems. In this framework, a deep understanding of the soil permeability in multi-level hydraulic fill areas can help to evaluate the stability of the soil and the design and construction of buildings and provide a scientific basis for ground settlement prevention and control.

As mentioned earlier, the permeability anisotropy of soil changes with the properties of the soil itself. Soils with different reclamation times and burial depths may have significant differences in permeability anisotropy due to their different soil-forming environments. The permeability anisotropy of the underlying cohesive soil in the CES area is significantly higher than that of dredger fill and sandy silt. To some extent, it indicates that the vertical drainage capacity of clay plays an increasingly important role in the consolidation settlement of newly formed land areas. Furthermore, the cohesive soil layer, as the main compression layer, is currently in the under-consolidated stage, and reaching the final consolidation stage requires a slow and long-term process [6]. Therefore, for engineering decision makers, the vertical drainage capacity needs to be given special attention.

5. Conclusions

This study focuses on the typical multi-level reclamation area of Chongming East Shoal in Shanghai as a research site. Through saturated variable-head permeability tests, qualitative and quantitative analysis of SEM images, and other physical and chemical tests, the anisotropic behavior and formation mechanism of permeability in soil layers near inland and offshore profiles have been explored. From the perspective of the effective seepage-pore area, new micro-parameters that respond to the permeability anisotropy have been established, providing a new method for assessing permeability anisotropy based on SEM images. The main conclusions are summarized below:

(1) The USC has higher permeability anisotropy than dredger fill and sandy silt, and its permeability anisotropy decreases with burial depth and reclamation time. The K_h and K_v values of dredger fill and sandy silt are relatively close, whereas the K_h of USC is higher than that of K_v. However, the advantage of K_h over K_v in inland USC is weakened compared with offshore USC. Meantime, the upper clay layer (21.5 m) has higher permeability anisotropy than the lower clay layer (41.5 m) in the thickest layer.

(2) An increase in the hydraulic gradient induces an increase in permeability anisotropy of USC, but the growth of the PAC fluctuates. With an increase in the hydraulic gradient, the K_h and K_v of the majority of the USC first increase and then decrease, and this phenomenon may even reoccur. A rise in the hydraulic gradient helps to unblock the seepage channels and increase permeability temporarily. Nevertheless, fine particles carried by the water may be trapped within the pores, causing temporary clogging of the seepage channels. With gradual increases in the hydraulic gradient, the opening and closing of seepage channels may occur repeatedly.

(3) Differences in the microstructure, particles, and pore parameters in the horizontal and vertical directions within a USC layer determine the spatiotemporal variability of anisotropic permeability. Among them, a simple soil framework and structure, strongly oriented arrangement of particles, decreased particle abundance, increased particle roundness, decreased particle contact area, and increased pore area are all factors that contribute to enhance permeability.

(4) From the perspective of the effective seepage-pore area, suitable micro-parameters for evaluating the permeability anisotropy have been established. Considering the restriction of bound water on the permeability efficiency of USC, pores with an area greater than 0.045 μm^2 are considered effective seepage channels. In comparison, when quantitatively evaluating the permeability anisotropy of USC from a micro-scale perspective, it may be more appropriate to use γ_{pw} as the variable for research.

Author Contributions: Conceptualization, M.Y.; methodology, Q.Y. and W.X.; formal analysis, Q.Y. and H.L.; writing—original draft preparation, M.Y.; writing—review and editing, Q.W.; project administration and funding acquisition, H.W., Q.W., X.H. and J.L. All authors have read and agreed to the published version of the manuscript.

Funding: This research was supported by the Shanghai Science and Technology Development Foundation (grant No. 20DZ1201200, 22ZR1447100, 21DZ2207400) and the National Natural Science Foundation (grant No. 42330708; 42302329).

Data Availability Statement: Data are contained within the article.

Acknowledgments: The authors would like to express their sincere thanks to the editor and anonymous reviewers for their professional comments and suggestions regarding this manuscript.

Conflicts of Interest: The authors declare no conflict of interest.

References

1. Manioudis, M.; Meramveliotakis, G. Broad strokes towards a grand theory in the analysis of sustainable development: A return to the classical political economy. *New Polit. Econ.* **2022**, *27*, 866–878. [CrossRef]
2. Klarin, T. The concept of sustainable development: From its beginning to the contemporary issues. *Zagreb Int. Rev. Econ. Bus.* **2018**, *21*, 67–94. [CrossRef]

3. Wang, W.; Liu, H.; Li, Y.Q.; Su, J.L. Development and management of land reclamation in China. *Ocean Coastal Manag.* **2014**, *102*, 415–425. [CrossRef]
4. Lai, W.C.; Lu, W.S.; Lorne, F. A catallactic framework of government land reclamation: The case of Hong Kong and Shenzhen. *Habitat Int.* **2014**, *44*, 62–71. [CrossRef]
5. Ganesalingam, D.; Arulrajah, A.; Ameratunga, J.; Boyle, P.J.; Sivakugan, N. Geotechnical properties of reconstituted dredged mud. In Proceedings of the Toronto 2011 Pan-Am CGS Geotechnical Conference, Toronto, ON, Canada, 2–6 October 2011; pp. 1–7.
6. Yu, Q.B.; Wang, Q.; Yan, X.X.; Yang, T.L.; Song, S.Y.; Yao, M.; Zhou, K.; Huang, X.L. Ground Deformation of the Chongming East Shoal Reclamation Area in Shanghai Based on SBAS-InSAR and Laboratory Tests. *Remote Sens.* **2020**, *12*, 1016. [CrossRef]
7. Li, X.A.; Li, L.C.; Song, Y.X.; Hong, B.; Wang, L.; Sun, J.Q. Characterization of the mechanisms underlying loess collapsibility for land-creation project in Shaanxi Province, China—A study from a micro perspective. *Eng. Geol.* **2019**, *249*, 77–88. [CrossRef]
8. Bolton, A.J.; Maltman, A.J.; Fisher, Q. Anisotropic permeability and bimodal pore-size distributions of fine-grained marine sediments. *Mar. Pet. Geol.* **2000**, *17*, 657–672. [CrossRef]
9. Ai, Z.Y.; Hu, Y.D. Multi-dimensional consolidation of layered poroelastic materials with anisotropic permeability and compressible fluid and solid constituents. *Acta Geotech.* **2015**, *10*, 263–273. [CrossRef]
10. Ai, Z.Y.; Wu, C. Plane strain consolidation of soil layer with anisotropic permeability. *Appl. Math. Mech.-Engl. Ed.* **2009**, *11*, 1437–1444. [CrossRef]
11. Yoon, H.Y.; Valocchi, A.J.; Werth, C.J. Effect of soil moisture dynamics on dense nonaqueous phase liquid (DNAPL) spill zone architecture in heterogeneous porous media. *J. Contam. Hydrol.* **2007**, *90*, 159–183. [CrossRef]
12. Wu, L.Z.; Zhang, L.M.; Zhou, Y.; Li, B.E. Analysis of multi-phase coupled seepage and stability in anisotropic slopes under rainfall condition. *Environ. Earth Sci.* **2017**, *76*, 469. [CrossRef]
13. Wang, X.W.; Xu, Y.S. Impact of the depth of diaphragm wall on the groundwater drawdown during foundation dewatering considering anisotropic permeability of aquifer. *Water* **2021**, *13*, 418. [CrossRef]
14. Ren, J.; Shen, Z.Z.; Yang, J.; Yu, C.Z. Back analysis of the 3D seepage problem and its engineering applications. *Environ. Earth Sci.* **2016**, *75*, 113. [CrossRef]
15. Tang, Y.; Chan, D.H.; Zhu, D.Z. Analytical solution for steady-state groundwater inflow into a circular tunnel in anisotropic soils. *J. Eng. Mech.* **2018**, *144*, 06018003. [CrossRef]
16. Ai, Z.Y.; Zhao, Y.Z.; Song, X.; Mu, J.J. Multi-dimensional consolidation analysis of transversely isotropic viscoelastic saturated soils. *Eng. Geol.* **2019**, *253*, 1–13. [CrossRef]
17. Li, X.A.; Li, L.C. Quantification of the pore structures of Malan loess and the effects on loess permeability and environmental significance, Shaanxi Province, China: An experimental study. *Environ. Earth Sci.* **2017**, *76*, 523. [CrossRef]
18. Yu, Q.B.; Yan, X.X.; Wang, Q.; Yang, T.L.; Lu, W.X.; Yao, M.; Dong, J.Q.; Zhan, J.W.; Huang, X.L.; Niu, C.C.; et al. A Spatial-Scale Evaluation of Soil Consolidation Concerning Land Subsidence and Integrated Mechanism Analysis at Macro-, and Micro-Scale: A Case Study in Chongming East Shoal Reclamation Area, Shanghai, China. *Remote Sens.* **2021**, *13*, 2418. [CrossRef]
19. Zhou, J.; Luo, L.H.; Hu, H.; Xu, J.; Jiang, Y.C. Effect of traffic load on permeability of remolded kaolin. In *Advances in Transportation Geotechnics IV*; Lecture Notes in Civil Engineering; Tutumluer, E., Nazarian, S., Al-Qadi, I., Qamhia, I.I., Eds.; Springer: Cham, Switzerland, 2021; Volume 166.
20. Adams, A.L.; Germaine, J.T.; Flemings, P.B.; Day-Stirrat, R.J. Stress induced permeability anisotropy of Resedimented Boston Blue Clay. *Water Resour. Res.* **2013**, *49*, 6561–6571. [CrossRef]
21. Wang, J.J.; Qiu, Z.F. Anisotropic hydraulic conductivity and critical hydraulic gradient of a crushed sandstone-mudstone particle mixture. *Mar. Geores. Geotechnol.* **2017**, *35*, 89–97. [CrossRef]
22. Dudoignon, P.; Gélard, D.; Sammartino, S. Cam-clay and hydraulic conductivity diagram relations in consolidated and sheared clay-matrices. *Clay Min.* **2004**, *39*, 267–279. [CrossRef]
23. Chen, W.Z.; Ma, Y.S.; Yu, H.D.; Li, F.F.; Li, X.L.; Sillen, X. Effects of temperature and thermally-induced microstructure change on hydraulic conductivity of boom clay. *J. Rock Mech. Geotech. Eng.* **2017**, *9*, 383–395. [CrossRef]
24. Cheng, Z.L.; Ning, Z.F.; Yu, X.F.; Wang, Q.; Zhang, W.T. New insights into spontaneous imbibition in tight oil sandstones with nmr. *J. Petro Sci. Eng.* **2019**, *179*, 455–464. [CrossRef]
25. Li, B.; Wong, R.C.K.; Heidari, S. A modified kozeny-carman model for estimating anisotropic permeability of soft mudrocks. *Mar. Pet. Geol.* **2018**, *98*, 356–368. [CrossRef]
26. Han, Y.; Wang, Q.; Liu, J.; Li, X.H. Seepage characteristics in unsaturated dispersive soil considering soil salinity and density impacts: Experimental and numerical combined study. *J. Hydrol.* **2022**, *614*, 128538. [CrossRef]
27. Hu, C.; Liu, X.L.; Jia, Y.G.; Duan, Z.B. Permeability anisotropy of methane hydrate-bearing sands: Insights from CT scanning and pore network modelling. *Comput. Geotech.* **2020**, *123*, 103568. [CrossRef]
28. Xu, B.H.; He, N.; Jiang, Y.B.; Zhou, Y.Z.; Zhan, X.J. Experimental study on the clogging effect of dredged fill surrounding the PVD under vacuum preloading. *Geotext. Geomembr.* **2020**, *48*, 614–624. [CrossRef]
29. Horpibulsuk, S.; Yangsukkaseam, N.; Chinkulkijniwat, A.; Du, Y.J. Compressibility and permeability of Bangkok clay compared with kaolinite and bentonite. *Appl. Clay Sci.* **2011**, *52*, 150–159. [CrossRef]
30. Clennell, M.B.; Hovland, M.; Booth, J.S.; Henry, P.; Winters, W.J. Formation of natural gas hydrates in marine sediments: 1. conceptual model of gas hydrate growth conditioned by host sediment properties. *J. Geophys. Res. Solid Earth* **1999**, *104*, 22985–23003. [CrossRef]

31. Yang, Y.L.; Aplin, A.C. Permeability and petrophysical properties of 30 natural mudstones. *J. Geophys. Res. Solid Earth* **2007**, *112*, B03206. [CrossRef]
32. Pusch, R.; Yong, R. Water saturation and retention of hydrophilic clay buffer-microstructural aspects. *Appl. Clay Sci.* **2003**, *23*, 61–68. [CrossRef]
33. Daigle, H.; Dugan, B. Permeability anisotropy and fabric development: A mechanistic explanation. *Water Resour. Res.* **2011**, *47*, 12517. [CrossRef]
34. Yu, Q.B.; Yan, X.X.; Wang, Q.; Yang, T.L.; Kong, Y.Y.; Huang, X.L.; Mehmood, Q. X-ray computed tomography-based evaluation of the physical properties and compressibility of soil in a reclamation area. *Geoderma* **2020**, *375*, 114524. [CrossRef]
35. *GB50021-2001*; Code for Investigation of Geotechnical Engineering. China Architecture & Building Press: Beijing, China, 2009.
36. Yan, X.X.; Shi, Y.J. Structure characteristic of engineering geology in Shanghai. *Shanghai Geol.* **2006**, *4*, 19–24. (In Chinese)
37. Zhang, W.L.; Shi, Y.J. Discussion on Shanghai Engineering Geological Division. *Shanghai Land Resour.* **2013**, *34*, 5–9. (In Chinese)
38. *GB/T 50123-2019*; Standard for Soil Test Methods. China Planning Press: Beijing, China, 2019.
39. Yang, J.; Wei, L. Collapse of loose sand with the addition of fines: The role of particle shape. *Geotechnique* **2012**, *62*, 1111–1125. [CrossRef]
40. *SY/T 5163-2010*; Analysis Method for Clay Minerals and Ordinary Non-Clay Minerals in Sedimentary Rocks by the X-ray Diffraction. Petroleum Industry Press: Beijing, China, 2010.
41. Krylov, A.A.; Stein, R.; Ermakova, L.A. Clay minerals as indicators of late quaternary sedimentation constraints in the Mendeleev Rise, Amerasian Basin, Arctic Ocean. *Lithol. Miner. Resour.* **2014**, *49*, 103–116. [CrossRef]
42. Wang, K.; Zang, J.; Wang, G.D.; Zhou, A.T. Anisotropic permeability evolution of coal with effective stress variation and gas sorption: Model development and analysis. *Int. J. Coal Geol.* **2014**, *130*, 53–65. [CrossRef]
43. Bagarello, V.; Sferlazza, S.; Sgroi, A. Testing laboratory methods to determine the anisotropy of saturated hydraulic conductivity in a sandy–loam soil. *Geoderma* **2009**, *154*, 52–58. [CrossRef]
44. Beckwith, C.W.; Baird, A.J.; Heathwaite, A.L. Anisotropy and depth-related heterogeneity of hydraulic conductivity in a bog peat laboratory measurements. *Hydrol. Proc.* **2003**, *17*, 89–101. [CrossRef]
45. Liu, C.; Shi, B.; Zhou, J.; Tang, C.S. Quantification and characterization of microporosity by image processing, geometric measurement and statistical methods: Application on SEM images of clay materials. *Appl. Clay Sci.* **2011**, *54*, 97–106. [CrossRef]
46. Li, X.; Zhang, L.M. Characterization of dual-structure pore-size distribution of soil. *Can. Geotech. J.* **2019**, *46*, 129–141. [CrossRef]
47. Sircar, J.; Ospina, C.E.; Camp, W. Reclamation for a Bulk and Container Terminal Complex in a High Seismicity Region. In Proceedings of the 14th Triennial International Conference on Ports—Gateways to a World of Opportunities (PORTS), New Orleans, LA, USA, 12–15 June 2016; pp. 557–566.
48. Ma, R.; Shi, J.S.; Zhang, C. Spatial and temporal variation of soil organic carbon in the North China Plain. *Environ. Monit. Assess.* **2018**, *190*, 357. [CrossRef] [PubMed]
49. Song, Y.Q.; Wu, C.J.; Ye, G.L. Permeability and anisotropy of upper shanghai clays. *Rock Soil Mech.* **2018**, *39*, 2139–2144.
50. Yao, M.; Wang, Q.; Yu, Q.B.; Wu, J.Z.; Li, H.; Dong, J.Q.; Xia, W.T.; Han, Y.; Huang, X.L. Mechanism Study of Differential Permeability Evolution and Microscopic Pore Characteristics of Soft Clay under Saturated Seepage: A Case Study in Chongming East Shoal. *Water* **2023**, *15*, 968. [CrossRef]
51. Zhang, Q.Y.; Qian, H.; Xu, P.P.; Hou, K.; Zhang, Y.T.; Qu, W.G.; Lin, T.; Chen, Y. Microscale evidence for and formation mechanisms of shear-strength anisotropy of a loess-paleosol sequence since the late Early Pleistocene: The case study of the Xiushidu profile, Southern Chinese loess Plateau. *Catena* **2022**, *213*, 106228. [CrossRef]
52. Li, X.A.; Hong, B.; Wang, L.; Li, L.C.; Sun, J.Q. Microanisotropy and preferred orientation of grains and aggregates (POGA) of the Malan loess in Yan'an, China: A profile study. *Bull. Eng. Geol. Environ.* **2020**, *79*, 1893–1907. [CrossRef]
53. Witt, K.J.; Brauns, J. Permeability-Anisotropy due to particle shape. *Geotech. Eng. Div. ASCE* **1983**, *109*, 1181–1187. [CrossRef]
54. Sufian, A.; Russell, A.R.; Whittle, A.J. Evolving pore orientation, shape and size in sheared granular assemblies. *Granul. Matter* **2019**, *21*, 4. [CrossRef]
55. Zheng, J.; Hryciw, R.D. Traditional soil particle sphericity, roundness and surface roughness by computational geometry. *Geotechnique* **2015**, *65*, 494–506. [CrossRef]
56. Zemenu, G.; Martine, A.; Roger, C. Analysis of the behaviour of a natural expansive soil under cyclic drying and wetting. *Bull. Eng. Geol. Environ.* **2009**, *68*, 421–436. [CrossRef]
57. Xu, P.P.; Zhang, Q.Y.; Qian, H.; Hou, K. Investigation into microscopic mechanisms of anisotropic saturated permeability of undisturbed Q2 loess. *Environ. Earth Sci.* **2020**, *79*, 412. [CrossRef]
58. Cho, G.C.; Dodds, J.; Santamarina, J.C. Particle shape effects on packing density, stiffness, and strength: Natural and crushed sands. *J. Geotech. Geoenviron. Eng.* **2006**, *133*, 591–602. [CrossRef]
59. Nouguier-Lehon, C.; Cambou, B.; Vincens, E. Influence of particle shape and angularity on the behaviour of granular materials: A numerical analysis. *Int. J. Numer. Anal. Methods Geomech.* **2003**, *27*, 1207–1226. [CrossRef]
60. Powers, M.C. A new roundness scale for sedimentary particles. *J. Sediment. Res.* **1953**, *23*, 117–119. [CrossRef]
61. Zheng, J.X.; Hryciw, R.D. Cross-anisotropic fabric of sands by wavelet-based simulation of human cognition. *Soils Found.* **2018**, *58*, 1028–1041. [CrossRef]
62. Camenen, B. Simple and general formula for the settling velocity of particles. *J. Hydraul. Eng. ASCE* **2007**, *133*, 229–233. [CrossRef]
63. Ren, X.W.; Zhao, Y.; Deng, Q.L.; Li, D.X.; Wang, D.B. A relation of hydraulic conductivity—Void ratio for soils based on kozeny-carman equation. *Eng. Geol.* **2016**, *213*, 89–97. [CrossRef]

64. Sun, L.Q.; Lu, J.X.; Guo, W.; Yan, S.W.; Jia, T.Q. Models to predict compressibility and permeability of reconstituted clays. *Geotech. Test. J.* **2016**, *39*, 324–330. [CrossRef]
65. Cui, D.S.; Xiang, W.; Cao, L.J.; Liu, Q.B. Experimental study on reducing thickness of adsorbed water layer for red clay particles treated by ionic soil stabilizer. *Chin. J. Geotech. Eng.* **2010**, *6*, 944–949. (In Chinese)
66. Chapuis, R.P.; Aubertin, M. On the use of the kozeny-carman equation to predict the hydraulic conductivity of soils. *Can. Geotech. J.* **2003**, *40*, 616–628. [CrossRef]
67. Pires, L.F.; Cooper, M.; Cássaro, F.A.M.; Reichardt, K.; Bacchi, O.O.S.; Dias, N.M.P. Micromorphological analysis to characterize structure modifications of soil samples submitted to wetting and drying cycles. *Catena* **2008**, *72*, 297–304. [CrossRef]
68. Jiang, X.W.; Wang, X.S.; Wan, L. Semi-empirical equations for the systematic decrease in permeability with depth in porous and fractured media. *Hydrogeol. J.* **2010**, *18*, 839–850. [CrossRef]
69. Berisso, F.E.; Schjønning, P.; Keller, T.; Lamandé, M.; Etana, A.; De Jonge, L.W.; Iversen, B.V.; Arvidsson, J.; Forkman, J. Persistent effects of subsoil compaction on pore size distribution and gas transport in a loamy soil. *Soil Tillage Res.* **2012**, *122*, 42–51. [CrossRef]